Supporting Information

Diradical Silver Derivative of Nitronyl Nitroxide: Synthesis, Structure, and Conformation-Dependent Magnetic Properties

Igor A. Zayakin [1], Dmitry E. Gorbunov [2], Pavel G. Shangin [1], Mikhail A. Syroeshkin [1], Pavel V. Dorovatovskii [3], Alexander A. Korlyukov [4], Roman A. Novikov [1], Debin Xia [5], Nina P. Gritsan [2,*] and Evgeny V. Tretyakov [1,*]

[1] N. D. Zelinsky Institute of Organic Chemistry, Russian Academy of Sciences, Leninsky Ave. 47, 119991 Moscow, Russia; zavnsc3@ioc.ac.ru (I.A.Z.); shangin@ioc.ac.ru (P.G.S.); syroeshkin@ioc.ac.ru (M.A.S.); roman@ioc.ac.ru (R.A.N.)

[2] V. V. Voevodsky Institute of Chemical Kinetics and Combustion, Siberian Branch of Russian Academy of Sciences, Institutskaya St. 3, 630090 Novosibirsk, Russia; gorbunov@kinetics.nsc.ru

[3] NRC Kurchatov Institute, 123182 Moscow, Russia; paulgemini@mail.ru

[4] A. N. Nesmeyanov Institute of Organoelement Compounds, Vavilova St. 28, 119991 Moscow, Russia; alex@xrlab.ineos.ac.ru

[5] State Key Laboratory of Space Power-Sources, School of Chemistry and Chemical Engineering, Harbin Institute of Technology, Harbin 150001, China; xia@hit.edu.cn (D.X.)

* Correspondence: tretyakov@ioc.ac.ru (E.T.); gritsan@kinetics.nsc.ru (N.G.)

Table of Contents

Section S1. Images of Crystals of [Ag–$(IPr)_2$][Ag–$(NN)_2$] and [Ag–$(IPr)_2$][Ag–$(NN)_2$]·$2H_2O$ ..S2

Section S2. NMR, IR, and HRMS Spectra S4

Section S3. XRD study.....S14

Section S4. Thermogravimetric (TGA) and Differential Thermal Analysis (DTA). Differential Scanning Calorimetry (DSC) S20

Section S5. Quantum Chemical Calculations S22

References for Supporting Information.....S27

Section S1. Images of Crystals of [Ag–$(IPr)_2$][Ag–$(NN)_2$] and [Ag–$(IPr)_2$][Ag–$(NN)_2$]·$2H_2O$

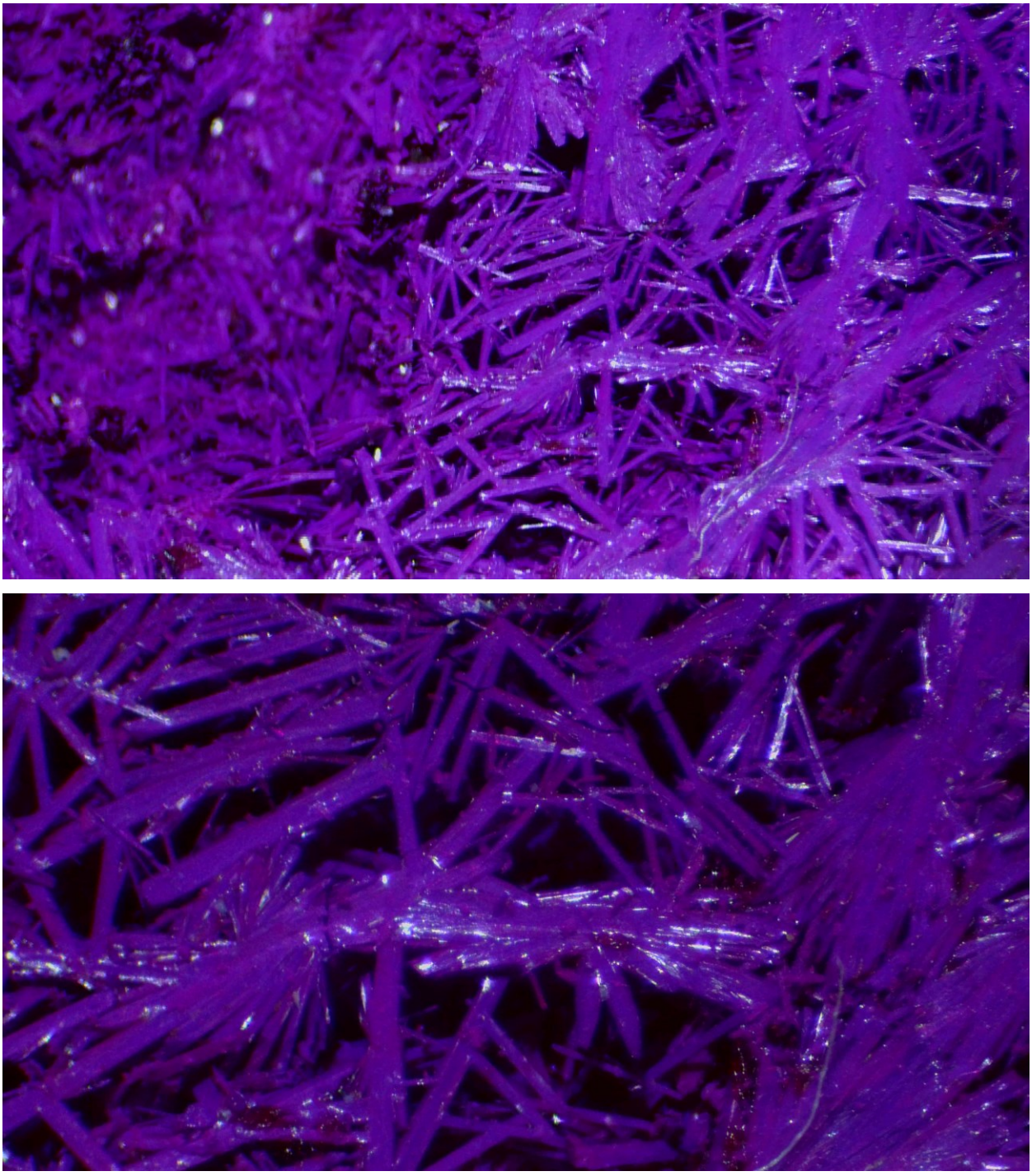


Figure S1. Optical microscope images of thin crystals of the organic silver derivative [Ag–$(IPr)_2$][Ag–$(NN)_2$] (the crystals were grown from a mixture of methylene chloride and *n*-heptane).

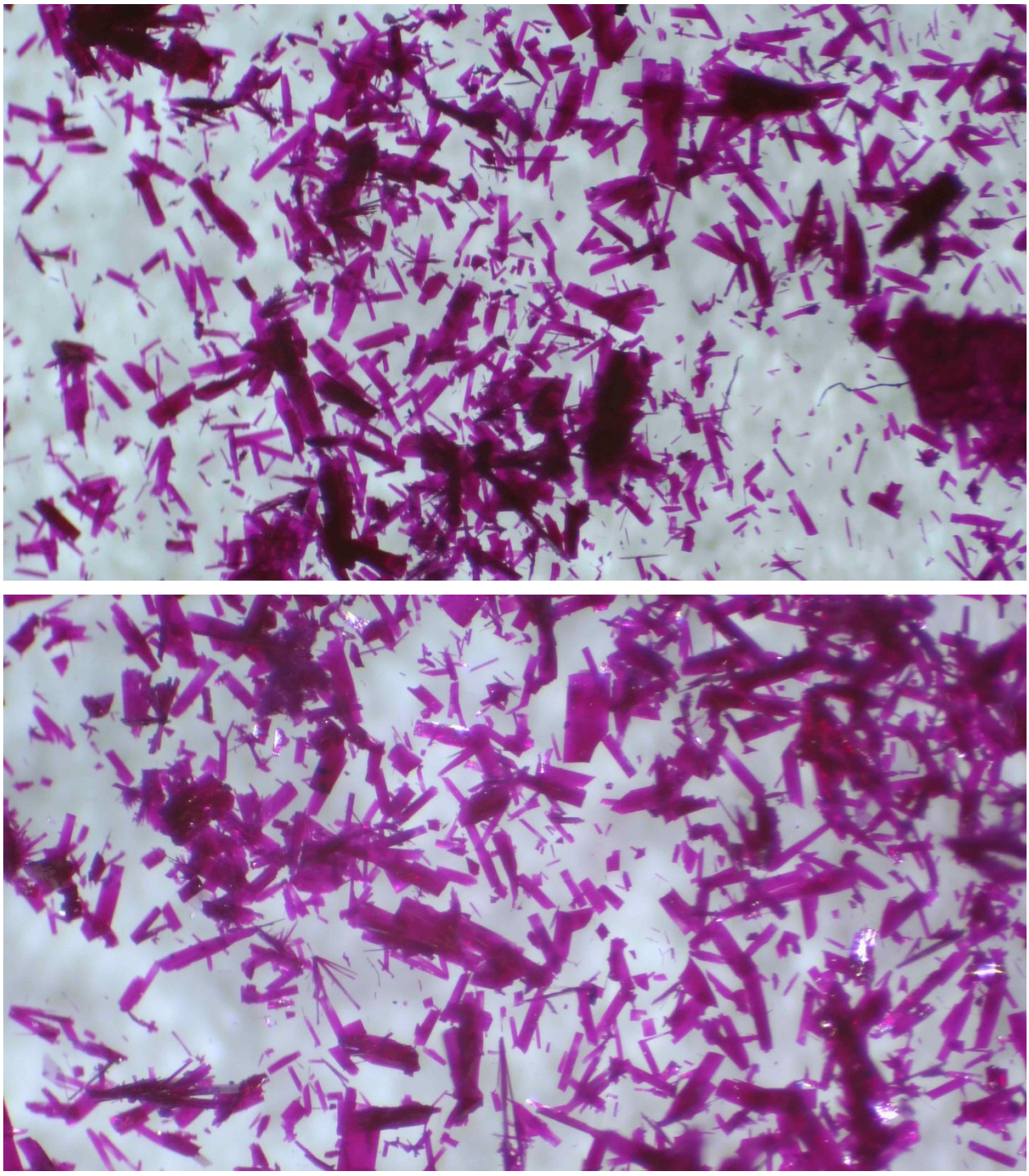
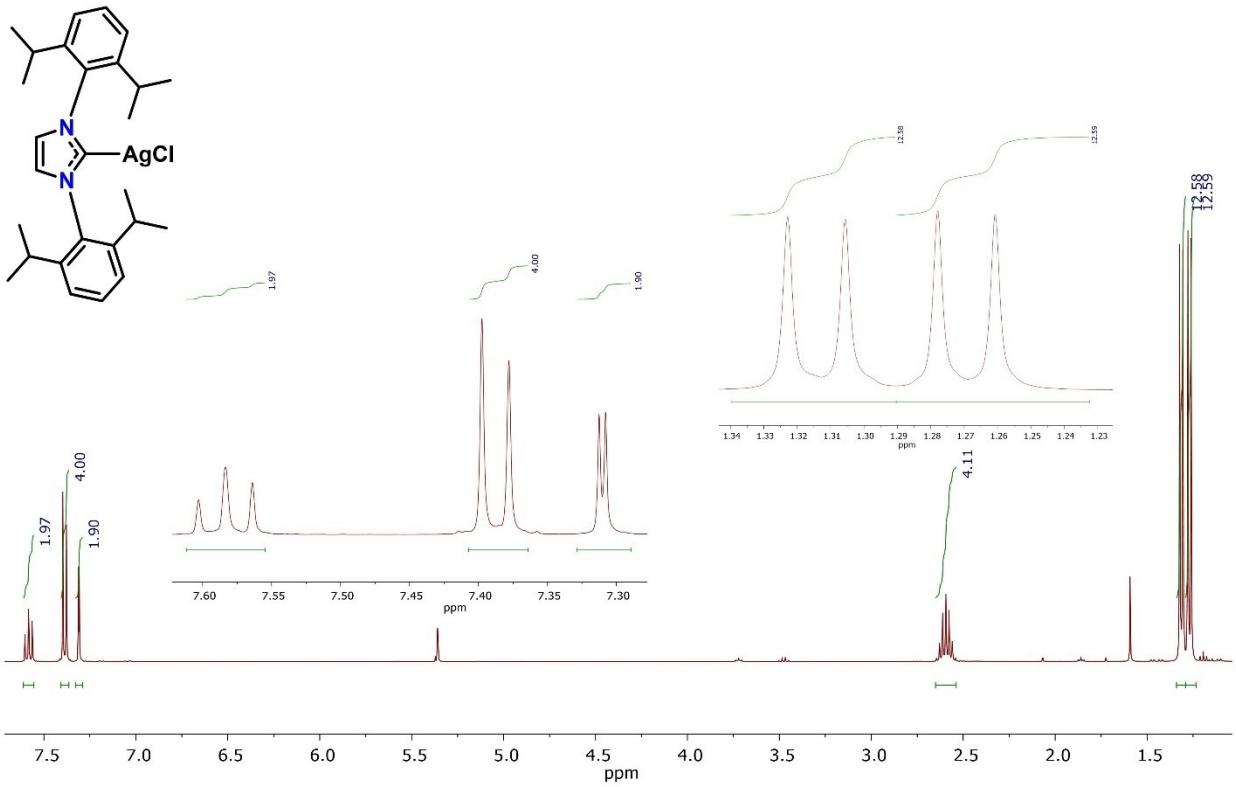
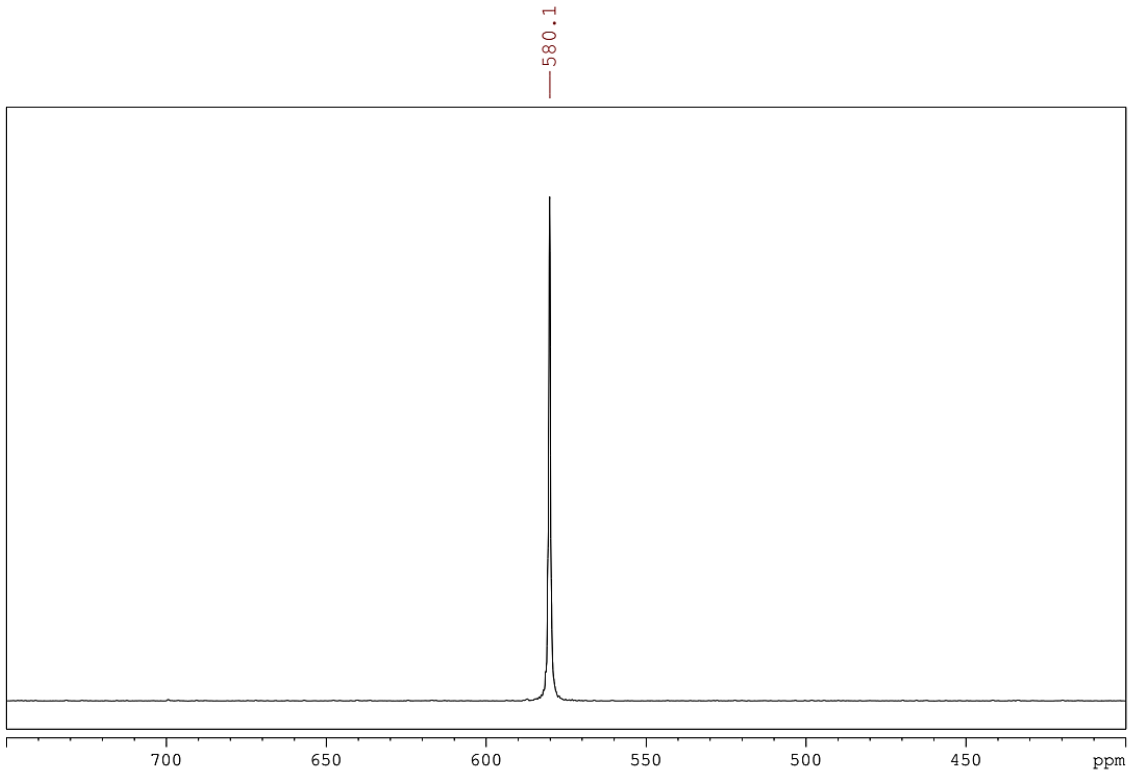


Figure S2. Optical microscope images of crystals of $[Ag–(IPr)_2][Ag–(NN)_2]\cdot 2H_2O$ (the crystals were grown from a mixture of acetone and benzene).

Section S2. NMR, IR, and HRMS Spectra





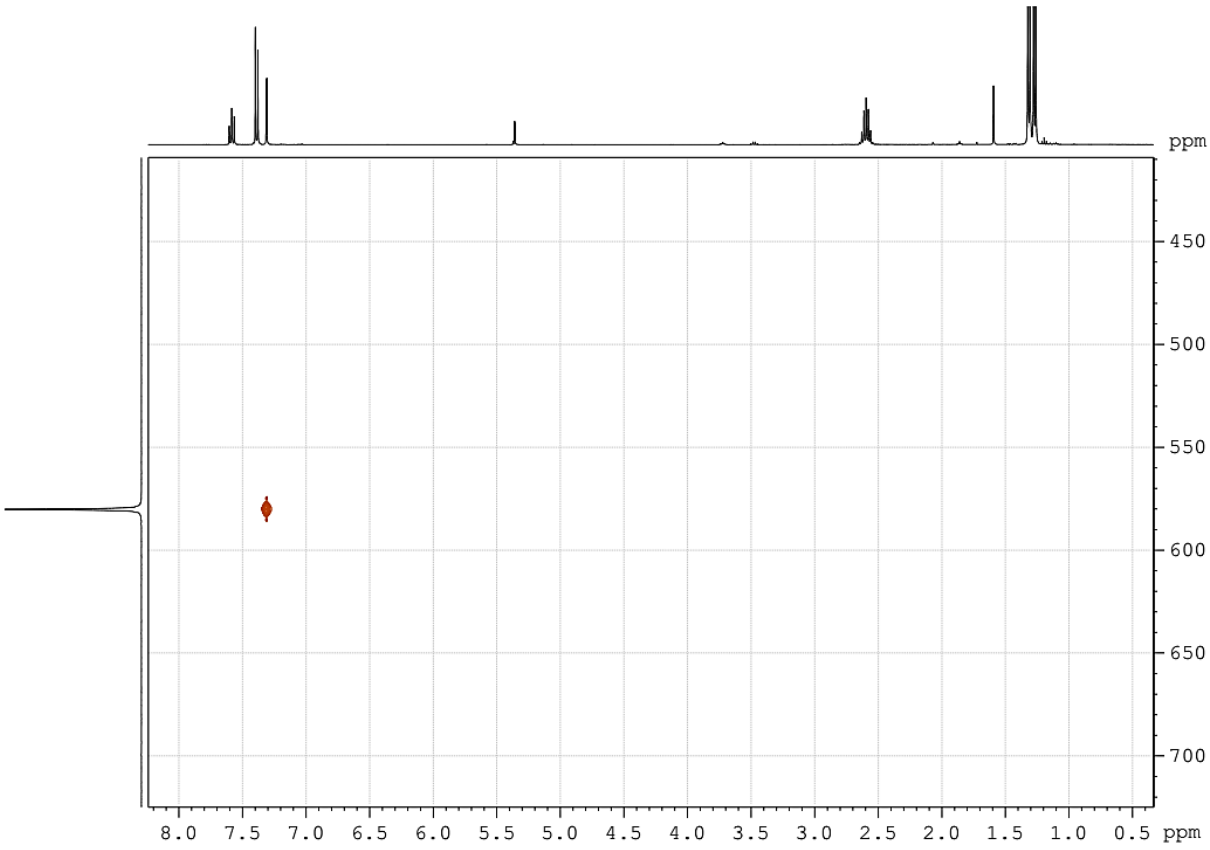
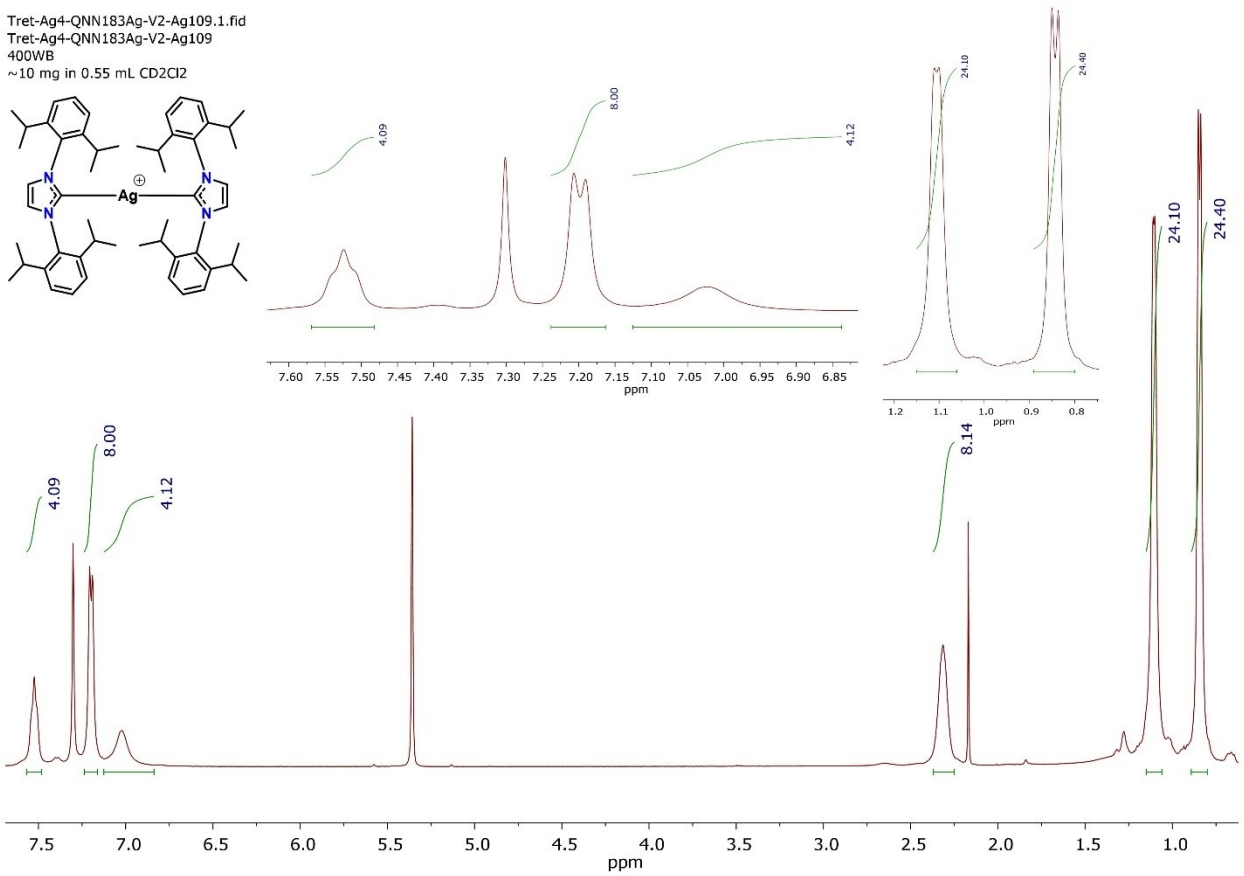
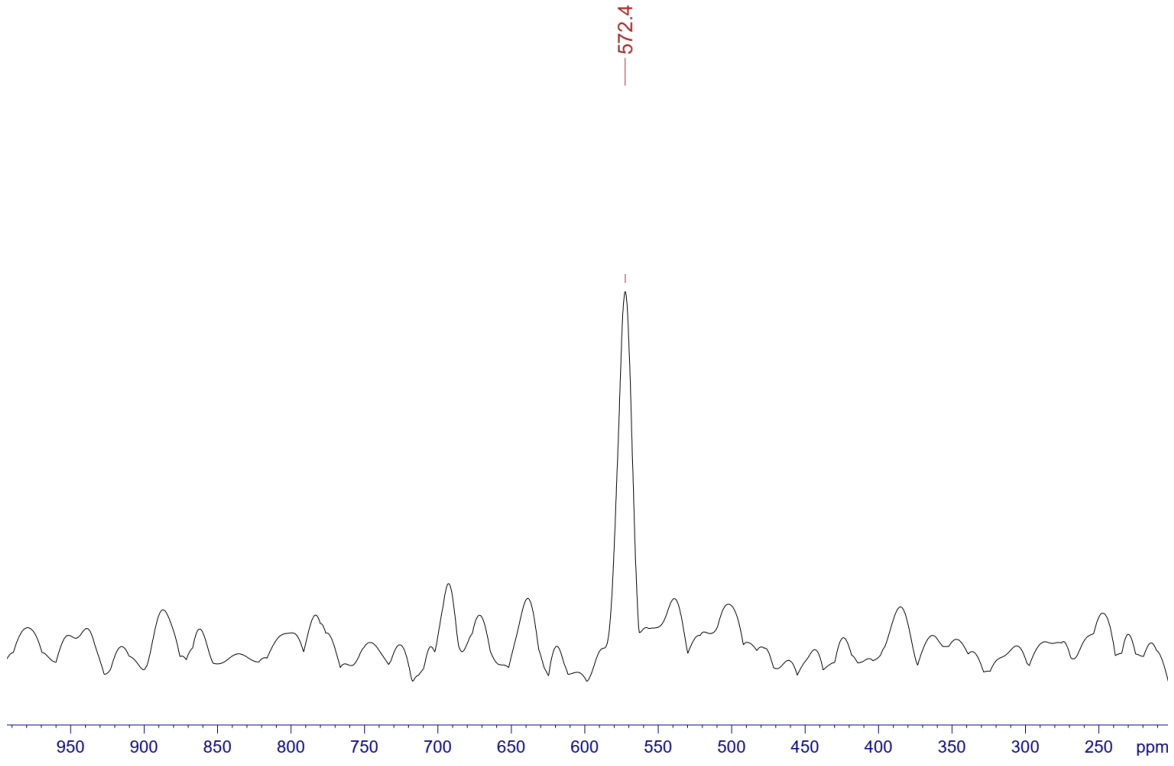


Figure S3. ^{109}Ag and ^{1}H-^{109}Ag HMBC NMR spectra of IPrAgCl in CD_2Cl_2 at 298 K.


Tret-Ag4-QNN183Ag-V2-Ag109.1.fid
Tret-Ag4-QNN183Ag-V2-Ag109
400WB
~10 mg in 0.55 mL CD2Cl2
Ag
4.09
8.00
4.12
8.14
24.10
24.40
ppm


572.4
ppm

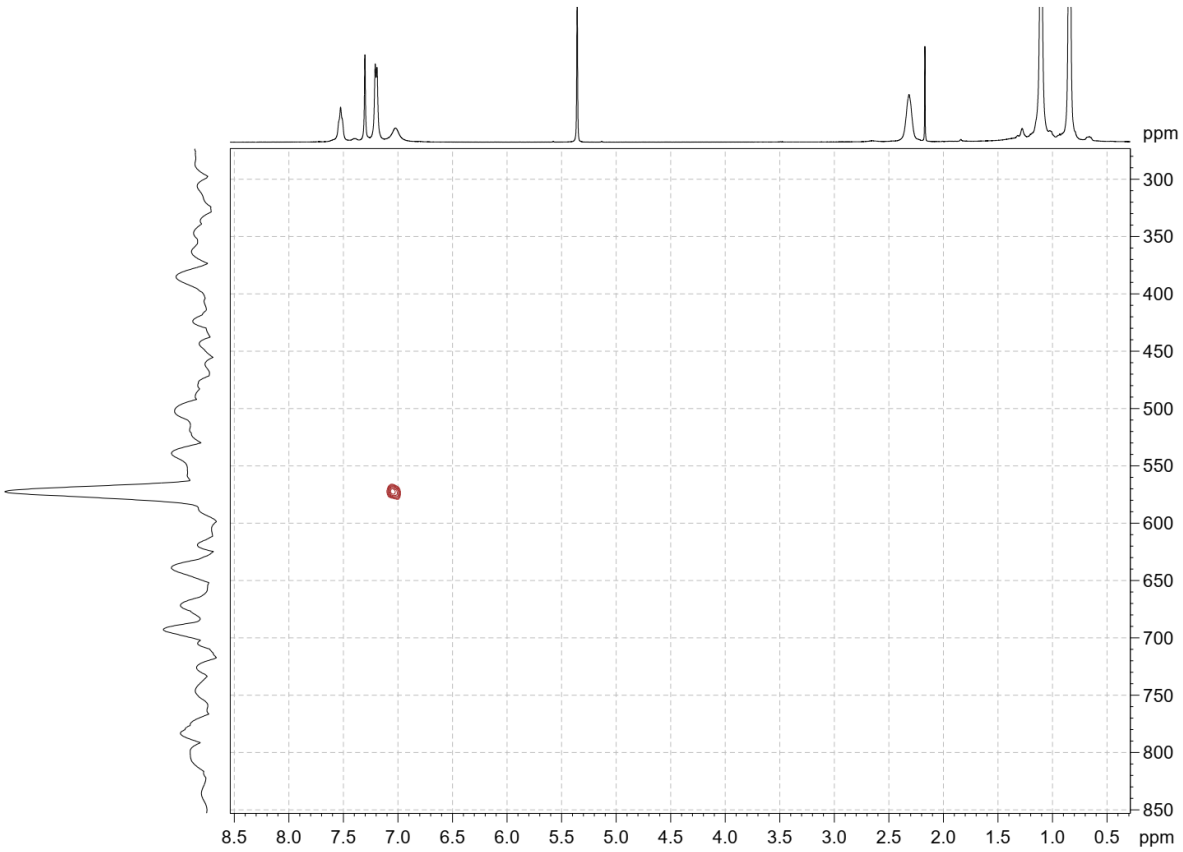


Figure S4a. ^{109}Ag and ^{1}H-^{109}Ag HMBC NMR spectra of [Ag–(IPr)$_2$][Ag–(NN)$_2$]·2H$_2$O in CD_2Cl_2 at 298 K.

The ^{109}Ag NMR chemical shifts for concentrated and dilute solutions differ significantly – by nearly 3 ppm – due to the influence of the radical at higher concentrations (as demonstrated in Evans' experiments). Correspondingly, the width of the associated ^{1}H NMR signal increases by more than a factor of two.

	Sample	^{109}Ag chemical shift, ppm
1	[Ag–(IPr)$_2$][Ag–(NN)$_2$]·2H$_2$O conc. – 6 mg in 0.55 mL CD_2Cl_2	**572.4**
2	[Ag–(IPr)$_2$][Ag–(NN)$_2$]·2H$_2$O diluted – 6 mg in 1.2 mL CD_2Cl_2	**569.7**

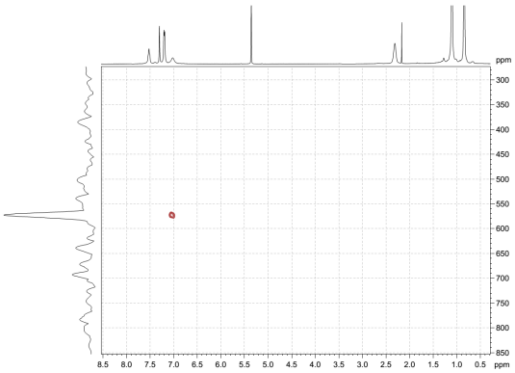
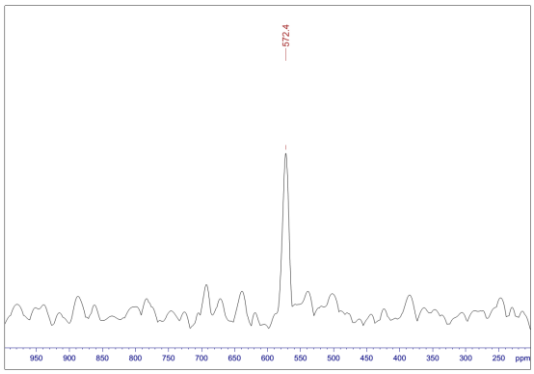
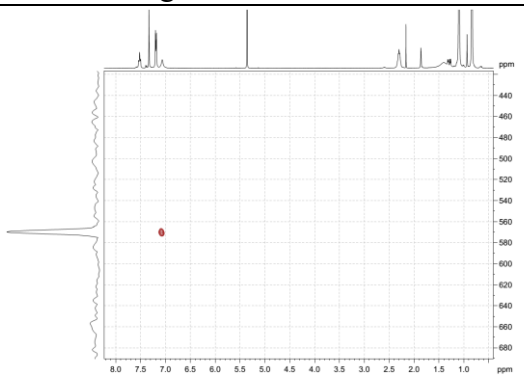
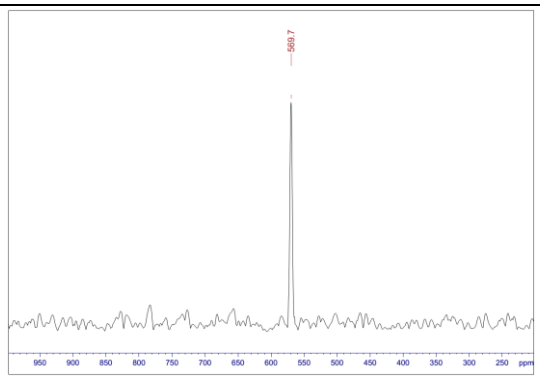
	^{1}H-^{109}Ag HMBC	^{109}Ag NMR spectrum (from HMBC)
1	[Ag–(IPr)$_2$][Ag–(NN)$_2$]·2H$_2$O conc. – 6 mg in 0.55 mL CD_2Cl_2	
		
2	[Ag–(IPr)$_2$][Ag–(NN)$_2$]·2H$_2$O diluted – 6 mg in 1.2 mL CD_2Cl_2	
		

Figure S4b. Influence of the concentration of [Ag–(IPr)$_2$][Ag–(NN)$_2$]·2H$_2$O on the ^{109}Ag signal broadening and chemical shift.

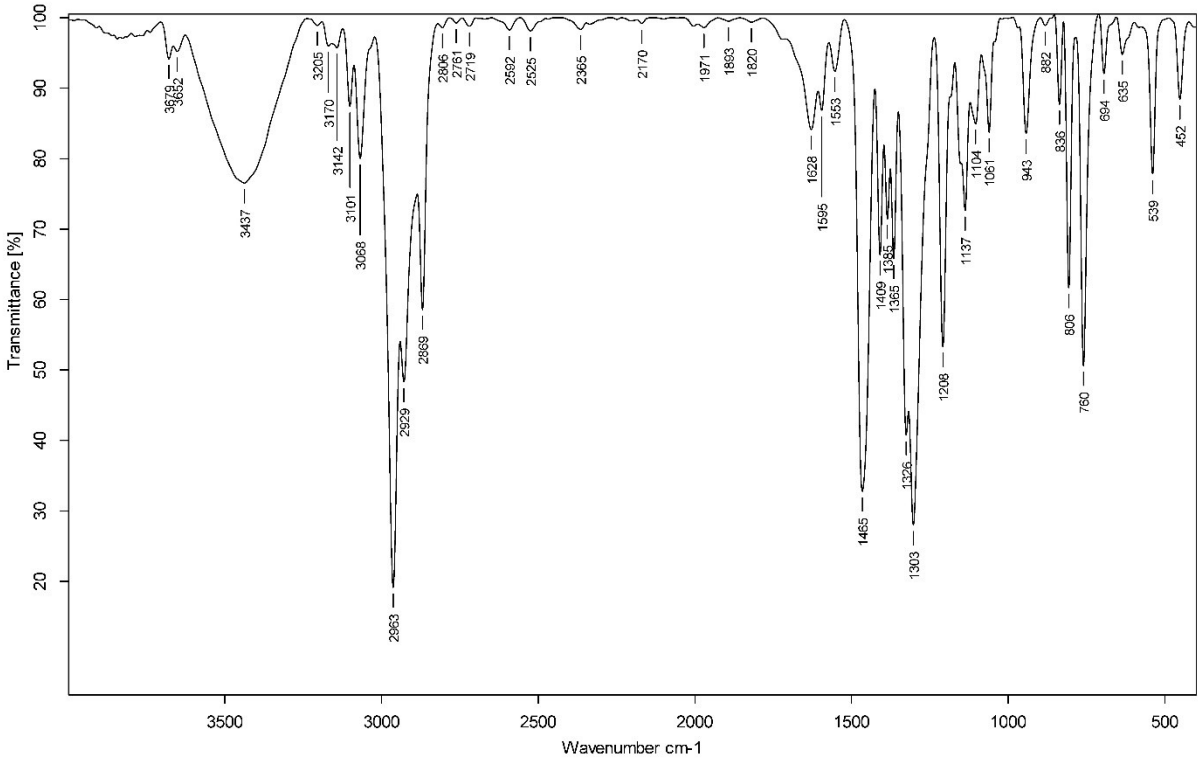


Figure S5. FT-IR spectrum of $[Ag–(IPr)_2][Ag–(NN)_2]\cdot 2H_2O$ recorded in KBr pellet.

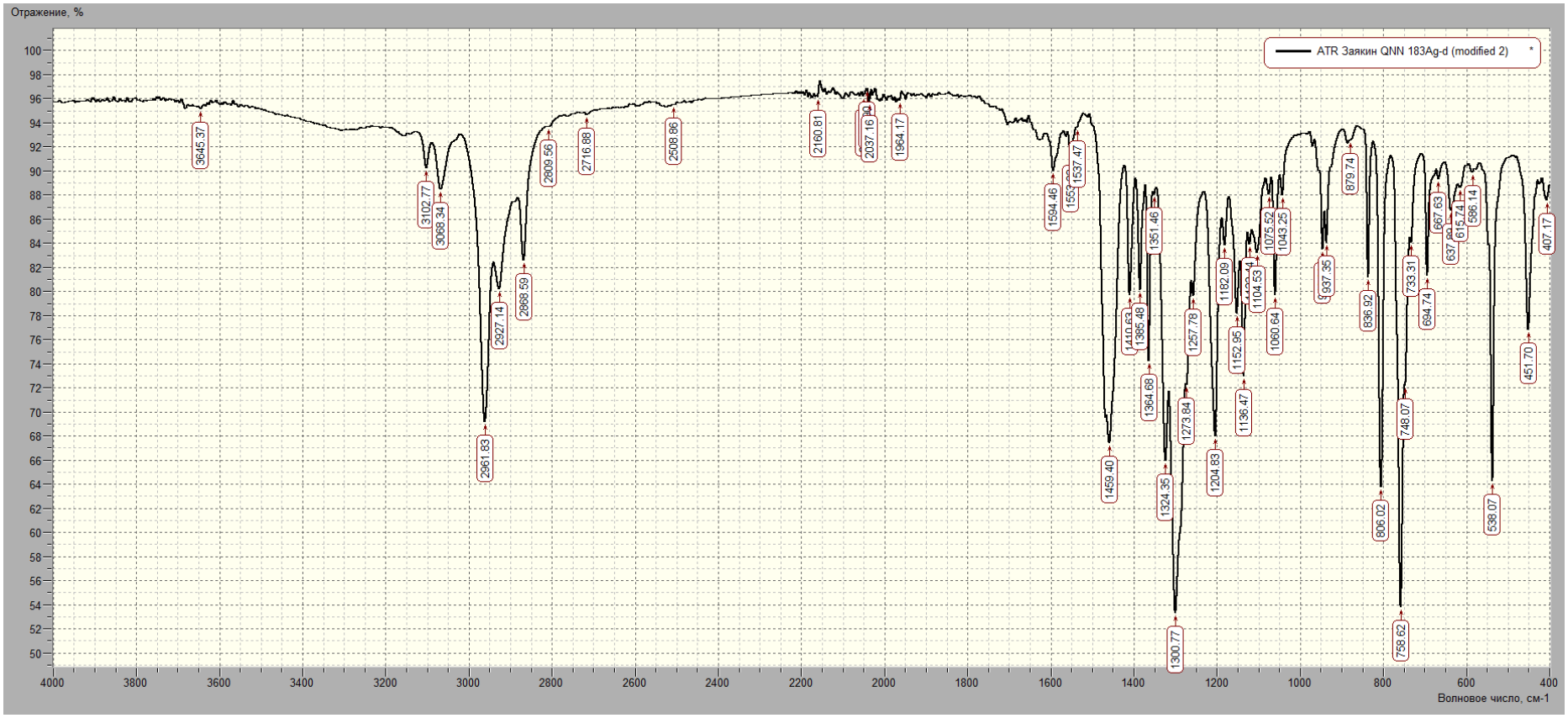


Figure S6a. Attenuated total reflection FT-IR spectrum of [Ag–$(IPr)_2$][Ag–$(NN)_2$].

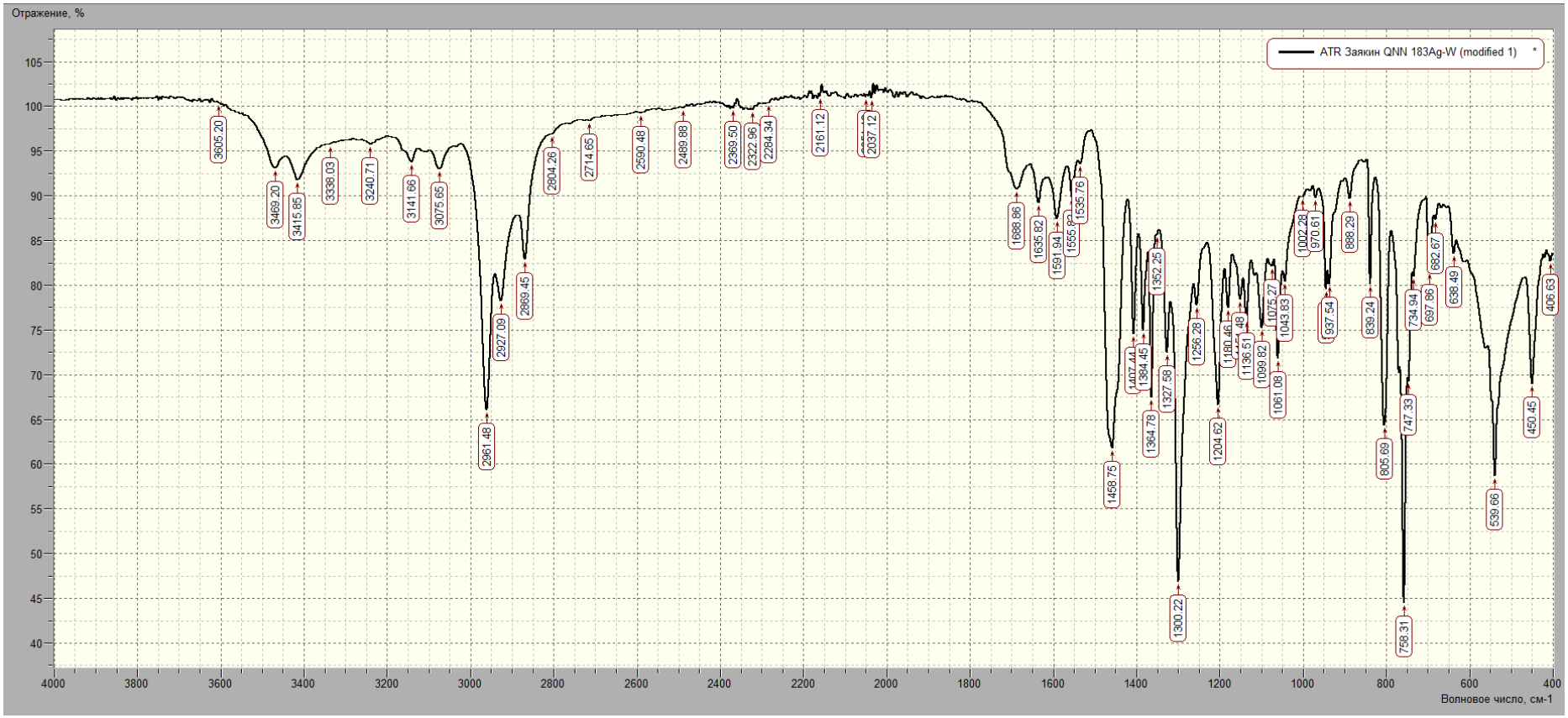


Figure S6b. Attenuated total reflection FT-IR spectrum of $[Ag–(IPr)_2][Ag–(NN)_2]\cdot 2H_2O$.

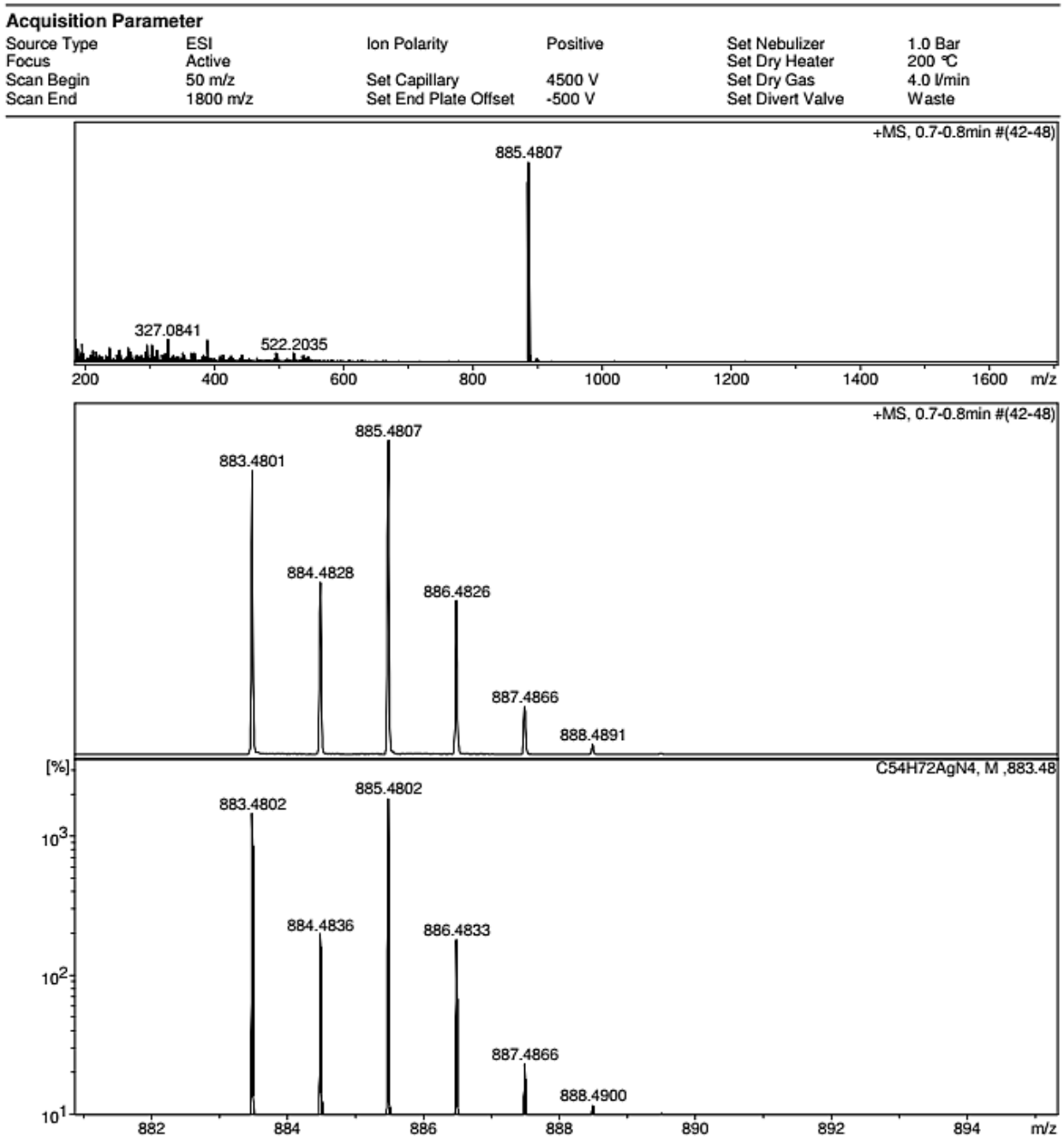


Figure S7a. ESI-HRMS spectrum of $[Ag–(IPr)_2][Ag–(NN)_2]$. In the negative ion mode, no MS peaks corresponding to the $[Ag–(NN)_2]^-$ ion were observed.

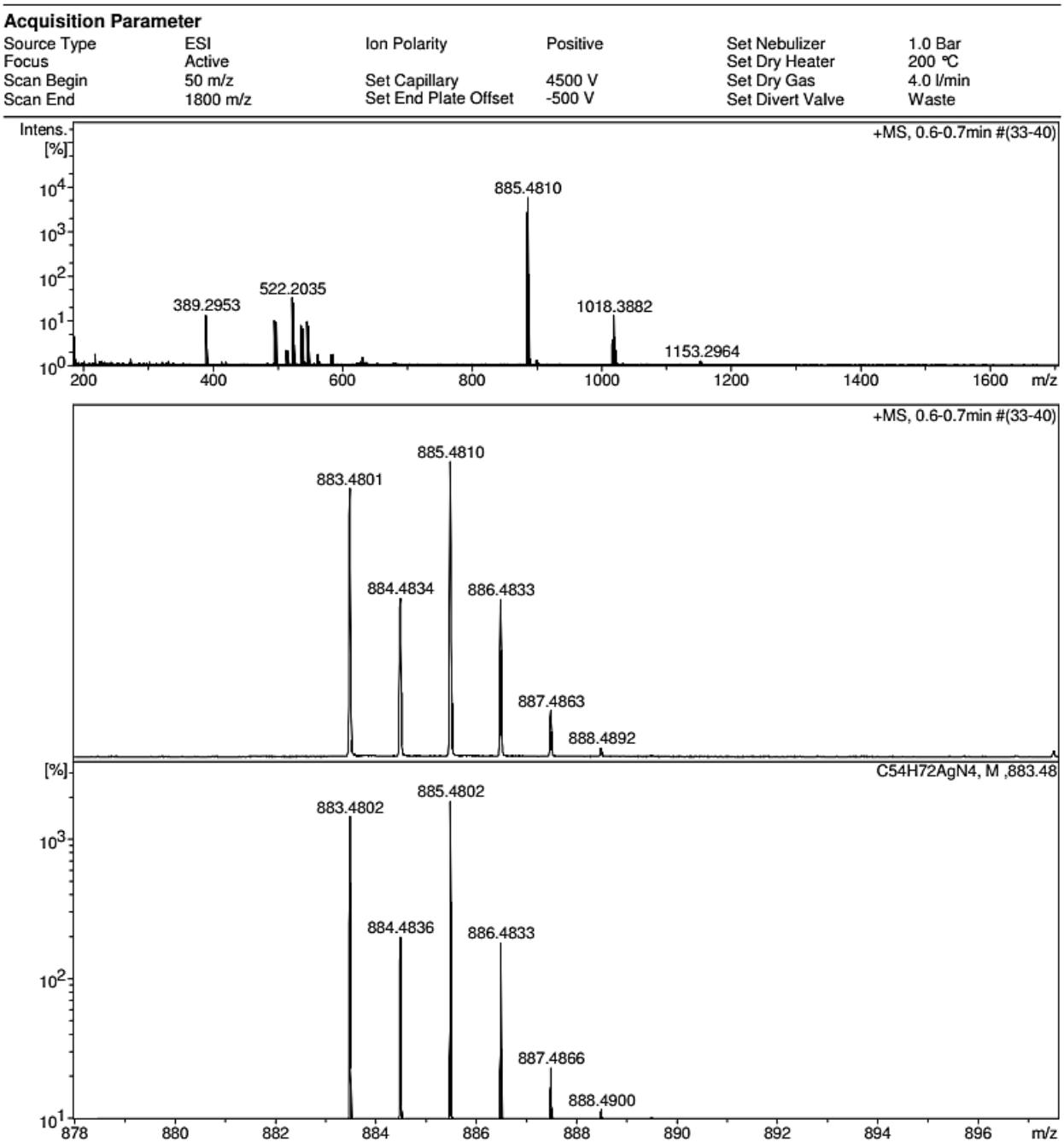


Figure S7b. ESI-HRMS spectrum of $[Ag–(IPr)_2][Ag–(NN)_2]\cdot 2H_2O$. In the negative ion mode, no MS peaks corresponding to the $[Ag–(NN)_2]^-$ or $\{[Ag–(NN)_2]\cdot 2H_2O\}^-$ ions were observed.

Section S3. XRD study

Table S1. Selected geometric parameters of $[Ag–(IPr)_2][Ag–(NN)_2]·2H_2O$.

Bond Lengths (Å)			
Ag01—C8	2.095(8)	C28—C29	1.517(13)
Ag01—C8^{i}	2.095(8)	C29—C30	1.505(9)
N3—C8	1.391(10)	C29—C31A	1.515(9)
N3—C10	1.397(9)	C29—C31B	1.496(10)
N3—C11	1.428(10)	C32—C33	1.494(13)
N4—C8	1.359(9)	C32—C34	1.518(13)
N4—C9	1.400(10)	Ag1—C1	2.084(8)
N4—C23	1.413(11)	Ag1—C1^{ii}	2.084(8)
C9—C10	1.328(11)	O1—N1	1.289(8)
C11—C12	1.386(11)	O2—N2	1.292(8)
C11—C16	1.409(11)	N1—C1	1.333(9)
C12—C13	1.397(12)	N1—C2	1.503(10)
C12—C17	1.524(12)	N2—C1	1.364(10)
C13—C14	1.374(13)	N2—C3	1.494(10)
C14—C15	1.370(14)	C2—C3	1.554(11)
C15—C16	1.387(12)	C2—C4	1.515(12)
C16—C20	1.510(13)	C2—C5	1.496(11)
C17—C18	1.531(15)	C3—C6	1.539(14)
C17—C19	1.526(14)	C3—C7	1.479(14)
C20—C21	1.506(14)	O1W—H1WA	0.8503
C20—C22	1.523(14)	O1W—H1WB	0.8511
C23—C24	1.391(12)	C24—C32	1.534(14)
C23—C28	1.382(13)	C25—C26	1.351(15)
C24—C25	1.346(13)	C26—C27	1.391(14)
		C27—C28	1.384(13)

Bond Angles (°)			
C8—Ag01—C8^{i}	179.3(4)	C30—C29—C28	110.4(9)

C8—N3—C10	110.6(6)	C30—C29—H29	106.4
C8—N3—C11	125.3(6)	C30—C29—C31A	115.4(13)
C10—N3—C11	124.1(7)	C31A—C29—C28	111.1(10)
C8—N4—C9	110.7(7)	C31A—C29—H29	106.4
C8—N4—C23	124.9(7)	C31B—C29—C28	132(2)
C9—N4—C23	124.2(7)	C24—C32—H32	108.0
N3—C8—Ag01	131.9(5)	C33—C32—C24	109.7(8)
N4—C8—Ag01	124.2(6)	C33—C32—H32	108.0
N4—C8—N3	103.8(6)	C33—C32—C34	110.8(8)
N4—C9—H9	126.0	C34—C32—C24	112.2(9)
C10—C9—N4	108.1(7)	C34—C32—H32	108.0
C10—C9—H9	126.0	C1—Ag1—C1^{ii}	180.0
N3—C10—H10	126.6	O1—N1—C1	125.4(7)
C9—C10—N3	106.8(7)	O1—N1—C2	118.2(6)
C9—C10—H10	126.6	C1—N1—C2	116.1(7)
C12—C11—N3	118.3(7)	O2—N2—C1	125.9(7)
C12—C11—C16	123.2(8)	O2—N2—C3	119.4(6)
C16—C11—N3	118.3(7)	C1—N2—C3	114.0(6)
C11—C12—C13	117.2(8)	N1—C1—Ag1	124.7(6)
C11—C12—C17	122.3(8)	N1—C1—N2	105.3(7)
C13—C12—C17	120.5(8)	N2—C1—Ag1	130.0(6)
C12—C13—H13	119.3	N1—C2—C3	99.4(6)
C14—C13—C12	121.3(9)	N1—C2—C4	106.1(6)
C14—C13—H13	119.3	C4—C2—C3	114.0(7)
C13—C14—H14	120.2	C5—C2—N1	111.3(7)
C15—C14—C13	119.6(8)	C5—C2—C3	114.5(7)
C15—C14—H14	120.2	C5—C2—C4	110.7(7)
C14—C15—H15	118.7	N2—C3—C2	101.3(6)
C14—C15—C16	122.6(9)	N2—C3—C6	105.4(7)
C16—C15—H15	118.7	C6—C3—C2	113.1(8)
C11—C16—C20	122.8(8)	C7—C3—N2	110.5(8)

C15—C16—C11	115.9(8)	C7—C3—C2	115.4(8)
C15—C16—C20	121.2(8)	C7—C3—C6	110.2(10)
C12—C17—H17	107.3	H1WA—O1W—H1WB	104.5
C12—C17—C18	113.1(9)	C25—C26—C27	119.9(9)
C12—C17—C19	114.8(9)	C25—C26—H26	120.0
C18—C17—H17	107.3	C26—C25—H25	119.6
C19—C17—H17	107.3	C24—C25—C26	120.8(9)
C19—C17—C18	106.8(9)	C24—C25—H25	119.6
C16—C20—H20	106.7	C25—C24—C32	120.2(9)
C16—C20—C22	111.0(8)	C25—C24—C23	119.1(10)
C21—C20—C16	115.7(9)	C23—C24—C32	120.7(8)
C21—C20—H20	106.7	C28—C23—C24	122.8(9)
C21—C20—C22	109.6(9)	C28—C23—N4	118.0(8)
C22—C20—H20	106.7	C24—C23—N4	119.1(8)
C27—C26—H26	120.0	C28—C29—H29	106.4
C26—C27—H27	119.2	C27—C28—C29	122.1(9)
C28—C27—C26	121.7(10)	C23—C28—C29	122.2(8)
C28—C27—H27	119.2	C23—C28—C27	115.7(9)

Torsion Angles (°)			
N3—C11—C12—C13	179.9(7)	C23—C24—C32—C33	−103.7(10)
N3—C11—C12—C17	2.7(12)	C23—C24—C32—C34	132.8(9)
N3—C11—C16—C15	−179.2(7)	C23—C28—C29—C30	127.8(12)
N3—C11—C16—C20	−0.6(12)	C23—C28—C29—C31A	−102.8(14)
N4—C9—C10—N3	2.3(9)	C23—C28—C29—C31B	−136(3)
N4—C23—C24—C25	177.2(7)	C24—C23—C28—C27	1.6(14)
N4—C23—C24—C32	−6.5(12)	C24—C23—C28—C29	179.4(8)
N4—C23—C28—C27	−174.5(8)	C24—C25—C26—C27	0.2(15)
N4—C23—C28—C29	3.3(13)	C25—C24—C32—C33	72.6(11)
C8—N3—C10—C9	−1.8(9)	C25—C24—C32—C34	−51.0(11)
C8—N3—C11—C12	78.5(10)	C25—C26—C27—C28	2.6(16)
C8—N3—C11—C16	−105.0(9)	C26—C27—C28—C23	−3.4(15)

C8—N4—C9—C10	−2.2(10)	C26—C27—C28—C29	178.7(10)
C8—N4—C23—C24	95.4(10)	C27—C28—C29—C30	−54.5(14)
C8—N4—C23—C28	−88.3(10)	C27—C28—C29—C31A	74.9(15)
C9—N4—C8—Ag01	178.6(6)	C27—C28—C29—C31B	42(3)
C9—N4—C8—N3	1.0(9)	C28—C23—C24—C25	1.1(13)
C9—N4—C23—C24	−89.6(10)	C28—C23—C24—C32	177.3(8)
C9—N4—C23—C28	86.7(11)	C32—C24—C25—C26	−178.3(9)
C10—N3—C8—Ag01	−176.9(6)	O1—N1—C1—Ag1	−1.2(12)
C10—N3—C8—N4	0.5(8)	O1—N1—C1—N2	−179.8(7)
C10—N3—C11—C12	−102.2(9)	O1—N1—C2—C3	168.8(7)
C10—N3—C11—C16	74.4(10)	O1—N1—C2—C4	−72.7(9)
C11—N3—C8—Ag01	2.5(12)	O1—N1—C2—C5	47.8(9)
C11—N3—C8—N4	179.9(7)	O2—N2—C1—Ag1	0.6(13)
C11—N3—C10—C9	178.8(7)	O2—N2—C1—N1	179.1(8)
C11—C12—C13—C14	−0.7(14)	O2—N2—C3—C2	170.7(8)
C11—C12—C17—C18	70.1(12)	O2—N2—C3—C6	−71.2(10)
C11—C12—C17—C19	−167.1(9)	O2—N2—C3—C7	47.9(12)
C11—C16—C20—C21	−153.9(8)	N1—C2—C3—N2	18.3(8)
C11—C16—C20—C22	80.4(11)	N1—C2—C3—C6	−94.0(8)
C12—C11—C16—C15	−2.8(12)	N1—C2—C3—C7	137.8(9)
C12—C11—C16—C20	175.8(8)	C1—N1—C2—C3	−16.3(9)
C12—C13—C14—C15	−2.7(15)	C1—N1—C2—C4	102.2(8)
C13—C12—C17—C18	−107.0(10)	C1—N1—C2—C5	−137.3(8)
C13—C12—C17—C19	15.8(14)	C1—N2—C3—C2	−18.2(9)
C13—C14—C15—C16	3.5(15)	C1—N2—C3—C6	99.9(9)
C14—C15—C16—C11	−0.8(13)	C1—N2—C3—C7	−141.1(9)
C14—C15—C16—C20	−179.4(9)	C2—N1—C1—Ag1	−175.7(5)
C15—C16—C20—C21	24.6(12)	C2—N1—C1—N2	5.7(10)
C15—C16—C20—C22	−101.1(11)	C3—N2—C1—Ag1	−169.8(6)
C16—C11—C12—C13	3.5(13)	C3—N2—C1—N1	8.7(10)
C16—C11—C12—C17	−173.7(9)	C4—C2—C3—N2	−94.1(8)

C17—C12—C13—C14	176.6(9)	C4—C2—C3—C6	153.6(8)
C23—N4—C8—Ag01	−5.8(11)	C4—C2—C3—C7	25.3(11)
C23—N4—C8—N3	176.6(7)	C5—C2—C3—N2	137.0(7)
C23—N4—C9—C10	−177.8(8)	C5—C2—C3—C6	24.7(10)
C23—C24—C25—C26	−2.0(13)	C5—C2—C3—C7	−103.5(10)

Symmetry codes: (i) −*x*+1, *y*, −*z*+3/2; (ii) −*x*+1/2, −*y*+3/2, −*z*+1.

Powder X-ray diffraction analysis. Prior to powder X-ray diffraction analysis, the [Ag–(IPr)$_2$][Ag–(NN)$_2$] sample was ground to a fine powder and placed on a Si(911) zero-background flat holder. All measurements were performed on a D8 Advance diffractometer (Bruker AXS) in Bragg-Brentano focusing geometry using CuKα radiation in the 2θ range from 3.2 to 60°, with a scan rate of 0.5 deg·min^{-1} and angular step of 0.02°. Two scans were performed, after which the diffraction pattern was processed using DIFFRACplus EVA (Bruker AXS GmbH DIFFRAC.EVA, Bruker AXS GmbH, Karlsruhe, Germany, 2011). The work with the X-ray diffraction pattern was carried out using the DIFFRAC TOPAS 5.0 software (Coelho, A. TOPAS 5.0, Bruker AXS GmbH, Karlsruhe, Germany, 2012).

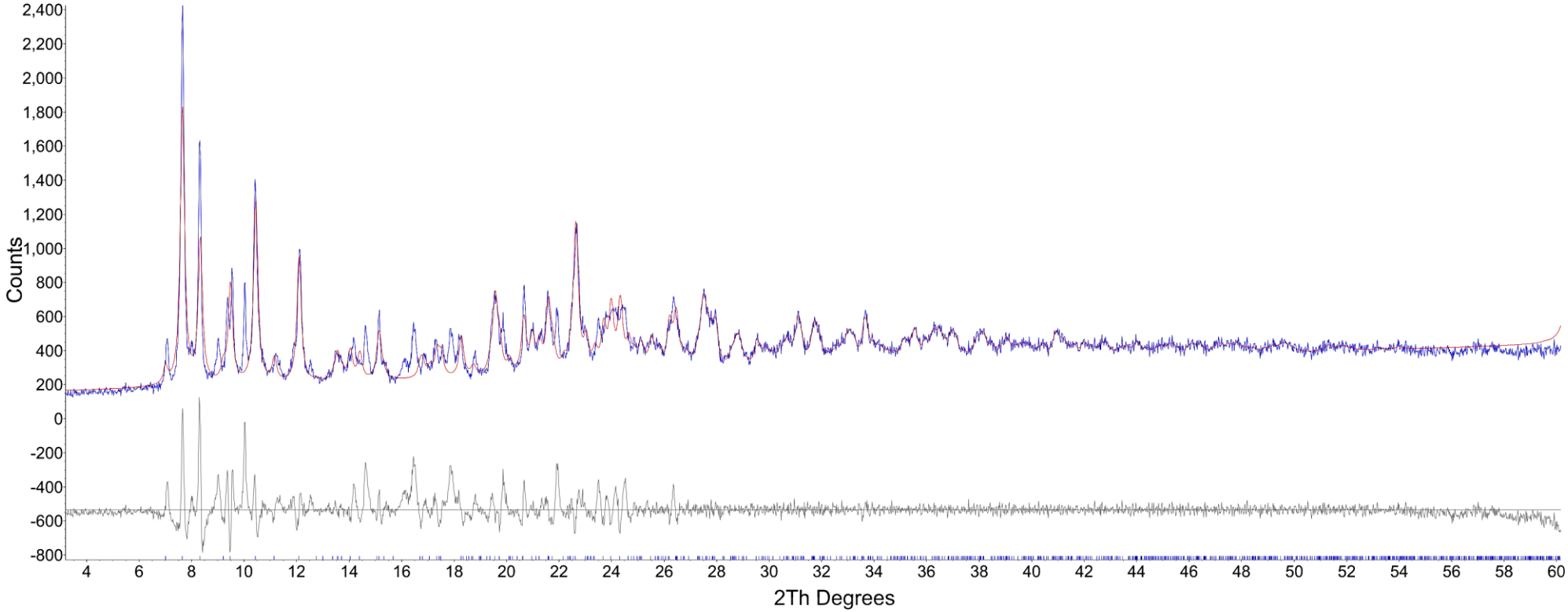


Figure S8. X-ray powder diffraction pattern of the $[Ag–(IPr)_2][Ag–(NN)_2]$ sample (blue curve). The red curve is calculated based on the data of the $[Ag–(IPr)_2][Ag–(NN)_2]\cdot 2H_2O$ single crystal. The gray curve is the difference between the two curves.

Section S4. Thermogravimetric (TGA) and Differential Thermal Analysis (DTA). Differential Scanning Calorimetry (DSC)

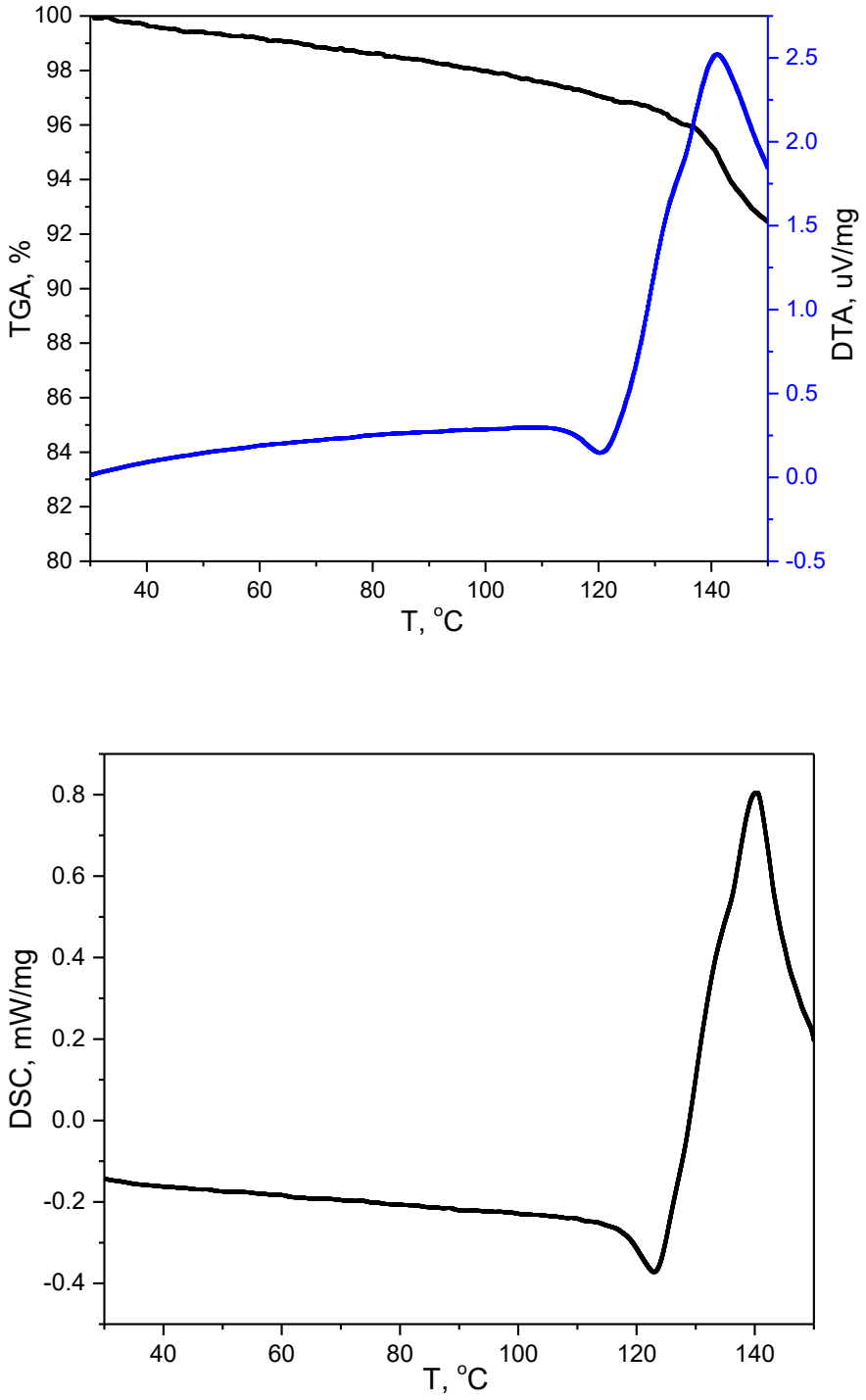


Figure S9. TGA-DTA and DSC curves of the $[Ag–(IPr)_2][Ag–(NN)_2]$ sample in the temperature range from 30 to 150 °C at a heating rate of 5 °C/min in an argon atmosphere.

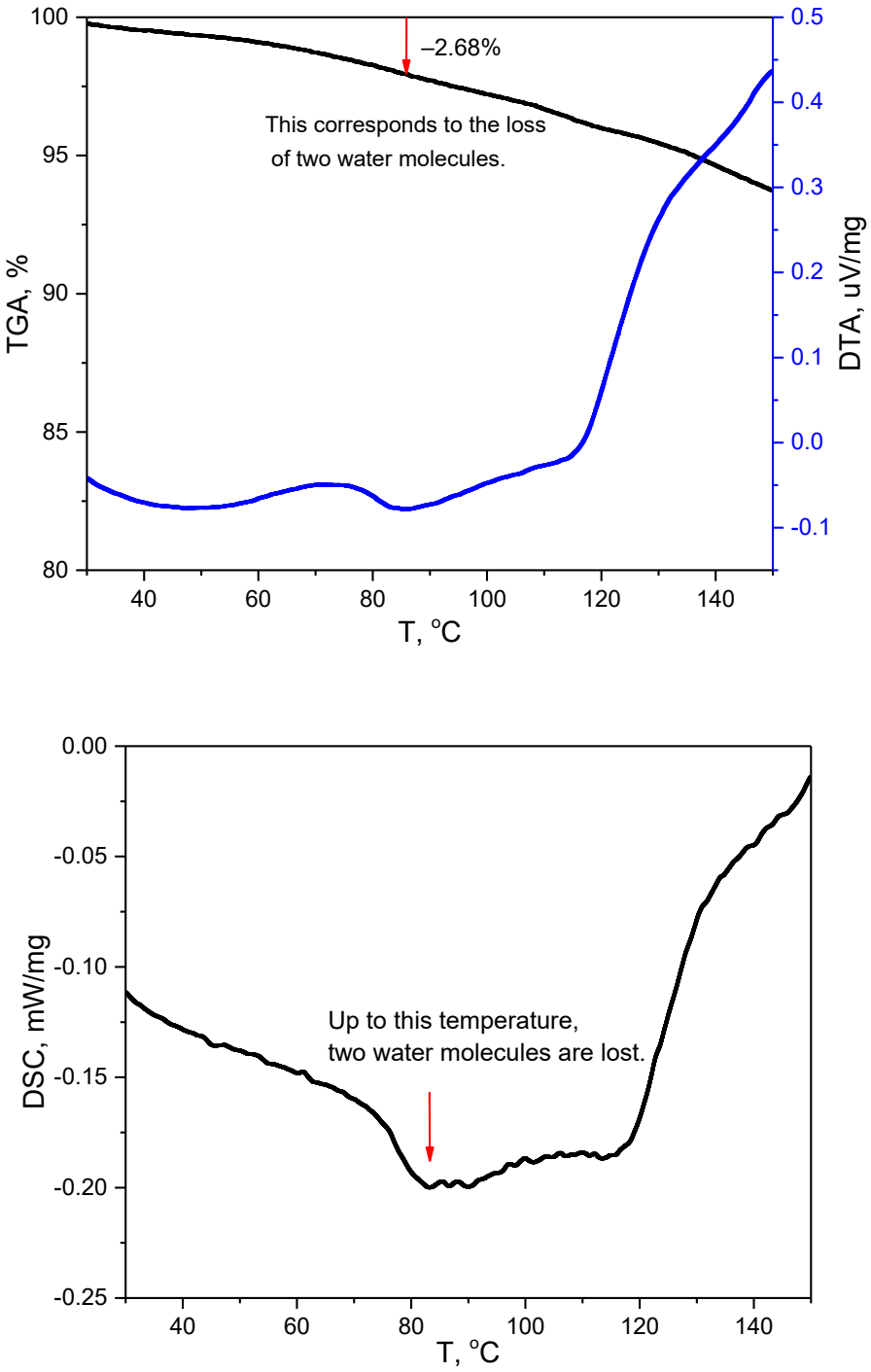


Figure S10. TGA-DTA and DSC curves of the $[Ag–(IPr)_2][Ag–(NN)_2]\cdot 2H_2O$ sample in the temperature range from 30 to 150 °C at a heating rate of 5 °C/min in an argon atmosphere.

Section S5. Quantum Chemical Calculations

S5.1. General

Geometry optimization of the $[Ag–(NN)_2]^-$ triplet diradical and its complexes with water was performed at the dispersion-corrected B97-D3 level [1] with the ma-def2-TZVPP basis set [2] with ECP for Ag [3]. The dispersion-corrected calculations were based on the Becke−Johnson damping function [4]. Optimizations were carried out taking into account toluene as a solvent using the CPCM model [5]. The ORCA 6.0.1 software package [6] was used for all calculations in this work.

For the $[Ag–(NN)_2]^-$ triplet diradical with optimized geometry, natural bond orbital (NBO) analysis [7] was performed using the NBO 7.0 software [8], as well as the results of all-electron DFT calculations using the scalar relativistic Douglas–Kroll–Hess (DKH2) Hamiltonian [9], the PBE0-D3 functional [2,10,11], and the ma-DKH-def2-TZVPP basis set for C, N and O atoms implemented in the ORCA 6.0.1 and SARS-DKH-TZVPP for Ag [12]. In the NBO procedure, $[Ag–(NN)_2]^-$ diradical was divided into three fragments: Ag^+ ion with the d^{10} valence shell and two NN anions as ligands. The strongly interacting NBOs were visualized in Chemcraf [13]. Orbital contributions to the Ag–C bond energies were calculated using the second-order perturbation theory. Moreover, the natural energy decomposition analysis (NEDA) [14] was performed using the NBO 7.0 software [8] and results of the DFT calculations at the same level of theory as for NBO analysis, but performed using the Gaussian 09 suit of programs [15].

The g-factor and HFC constants with ^{14}N and ^{107}Ag nuclei were also calculated at the all-electron DFT level using a hybrid TPSSh functional, combining 10% HF exchange and meta-GGA TPSS functional [16], and relativistic basis set described above. The spin-orbit coupling (SOC) was taken into account using the spin-orbit mean-field (SOMF) approximation [17]. Parameter J of the exchange interaction ($\hat{H} = -2J\hat{\vec{S}}_1\hat{\vec{S}}_2$) between radical fragments of the $[Ag–(NN)_2]^-$ diradical was calculated by the spin-unrestricted broken-symmetry approach [18] at the DKH2-UB3LYP level [19,20] with the same relativistic basis set as above, using the Yamaguchi formula [21].

S5.2. Optimization of the $[Ag–(NN)_2]^-$ diradical structure

To understand the properties of $[Ag–(IPr)_2][Ag–(NN)_2]$ salt, especially its quite unexpected ESR spectrum, we performed a series of DFT calculations. Since most of the measurements were performed in solution, we first optimized the geometry of the $[Ag–(NN)_2]^-$ diradical and its complexes with one and two waters in toluene. Comparison of XRD (Figure S11a) and optimized (Figure S11b) structures of complex with two waters shows that optimization leads to a small but noticeable change in the geometry of the complex. Specifically, the O···H hydrogen bonds become significantly shorter (by 0.04–0.07 Å), and the O···H–O angles become larger (by 7–10°), which are more typical of such hydrogen bonds. However, optimization does not disrupt the coplanarity of the NN fragments.

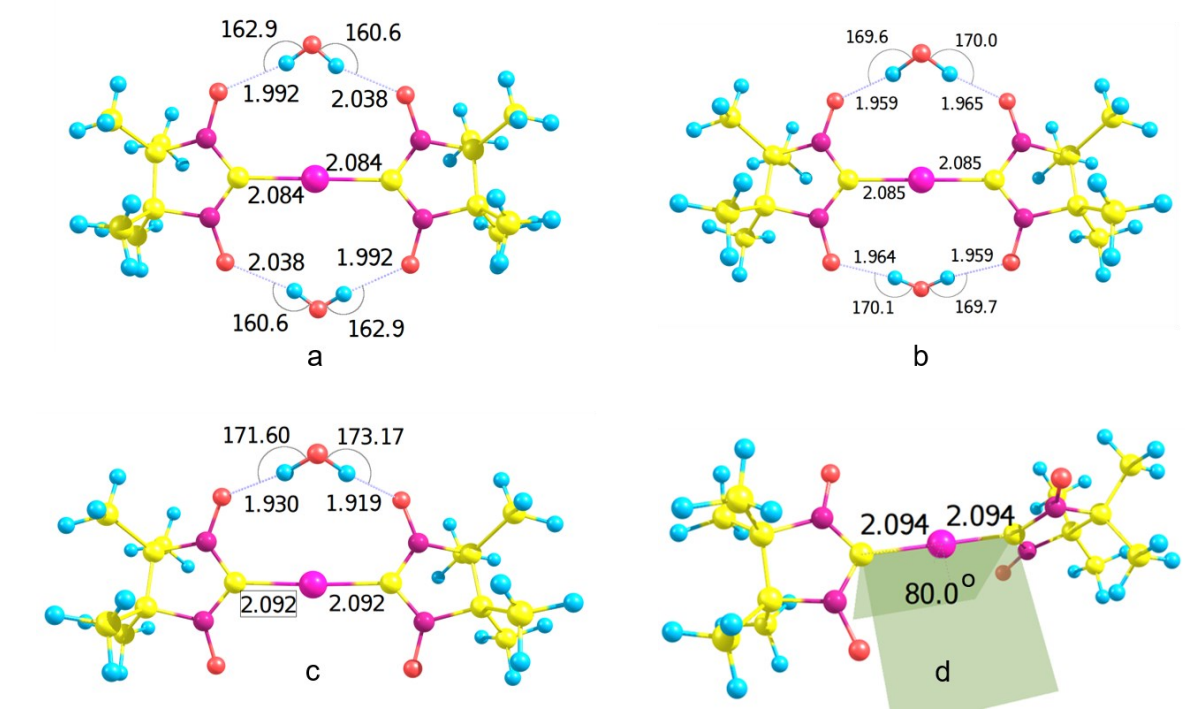


Figure S11. Experimental X-ray structure of the diradical complex with two water molecules (a), its structure optimized at the B97-D3/ma-def2-TZVPP level in toluene. As well as optimized structures with one water (c) and without water (d).

The removal of one water molecule from the complex (Figure S11c) also does not lead to significant change in the geometry of the diradical; the coplanarity of the NN fragments is preserved. On the contrary, removal of both water molecules from the complex leads to a significant change in the diradical structure (Figure S11d). Figure S11d shows that the minimum on the potential energy surface (PES) for the $[Ag–(NN)_2]^-$ diradical corresponds to a nearly

perpendicular arrangement of the NN fragments, while the coplanar arrangement of NN fragments corresponds to a transition state between two similar minima (Figure S12a).

The thermodynamics of the successive steps of the formation of final complex with two water molecules was calculated in toluene solution at the UB97-D3/def2-TZVPP level.

$$[Ag–(NN)_2]^- + H_2O \rightleftharpoons [Ag–(NN)_2]^-\cdot H_2O \quad \Delta G_1$$

$$[Ag–(NN)_2]^-\cdot H_2O + H_2O \rightleftharpoons [Ag–(NN)_2]^-\cdot 2H_2O \quad \Delta G_2$$

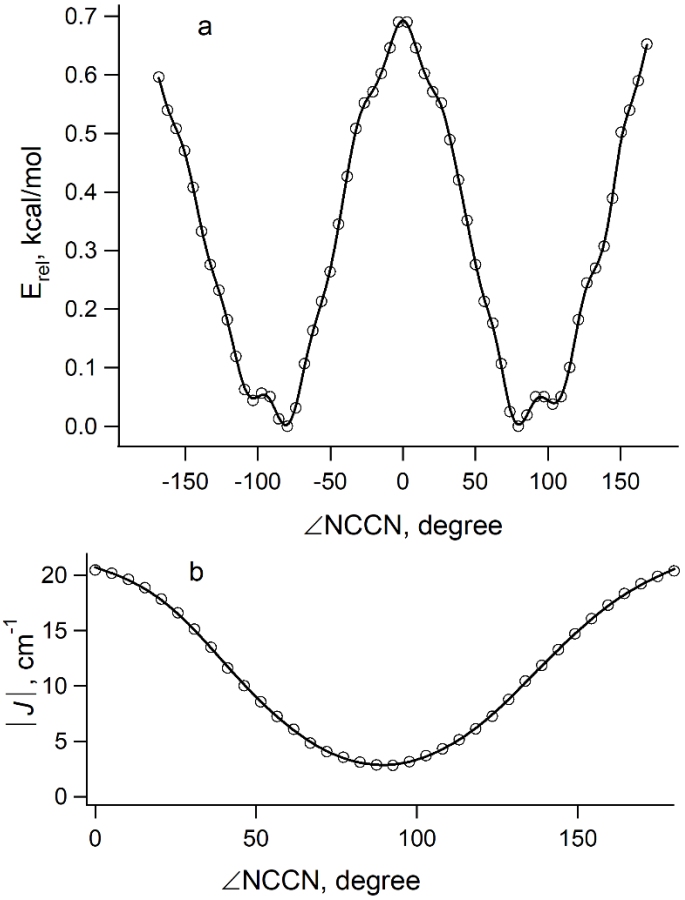


Figure S12. a) The energy scan performed at the UB97-D3/def2-TZVP level by varying the dihedral angle with optimization of all other coordinates for the rotation of one NN fragment around Ag–C bond for the $[Ag–(NN)_2]^-$ diradical in the triplet state. b) Absolute values of the parameter *J* of the exchange interaction between NN fragments calculated at the BS-UB3LYP/def2-TZVP level for diradical geometries varying along the right-hand side of the scan curve.

According to calculations, both steps of complex formation are endothermal, with free energies of complexation of 1.0 and 0.9 kcal/mol for ΔG_1 and ΔG_2, respectively (standard state, 1

M solution). Estimates using these values show that even in a water-saturated toluene solution (0.033% or 1.6×10^{-2} mol/L of H_2O), the concentrations of both type complexes are negligible.

S5.3. Calculations of exchange interaction between NN fragments

For the complexes of the $[Ag–(NN)_2]^-$ diradical with one and two waters (Figure S11a,c), we estimated the exchange interaction ($\hat{H} = -2J\hat{\vec{S}}_1\hat{\vec{S}}_2$) between the NN fragments, which were found to be antiferromagnetic (AF) and moderate with J value equal to –18.7 cm^{-1} for both at the BS-UB3LYP level. We also analyzed the change in the exchange interaction in the $[Ag–(NN)_2]^-$ diradical as a function of its geometry along the scanning curve (Figure S12a). Figure S12b shows that the value of parameter $|J|$ decreases by about an order of magnitude when moving along the PES from the coplanar NN arrangement (transition state) to the minimum (almost perpendicular arrangement). Although J value at the minimum was predicted to be small enough (about –3 cm^{-1}), it's still very large on the EPR scale. However, it is quite likely that the BS-DFT calculations slightly overestimate the value of J, and that it is actually low even on the EPR scale.

S5.4. Calculation of the spin-Hamiltonian parameters

The calculations of the g-tensor and HFC constants with ^{14}N and ^{107}Ag nuclei were performed at the all-electron DFT level using the scalar relativistic DKH2 Hamiltonian and perturbative treatment of spin-orbit coupling. Various exchange-correlation functionals were used for calculations. As for many other systems [22,23], the use of GGA functionals led to an underestimation of HFC with N atoms. More balanced results were obtained in calculations with hybrid functionals, so the use of the TPSSh hybrid meta-GGA functional leads to the following parameters: g_{iso} = 2.0070, $a(^{107}Ag)$ = –0.705 mT, $a(^{109}Ag)$ = –0.810 mT, and $a(^{14}N)$ = 0.559 ÷ 0.566 mT. The contribution of spin-orbit coupling to the HFC constants was 1.7% for Ag and 0.04% for N. It can be seen that the predicted values of $a(^{14}N)$ for all four nuclei are practically identical.

S5.5. The NBO and NEDA analysis of electronic structure

Modeling of the EPR spectrum (Figure 5, main text) gives a fairly high HFC constant with the Ag nucleus. To understand the electronic structure of the $[Ag–(NN)_2]^-$ complex, in particular the origin of the HFC constant with Ag nuclei, an analysis of $Ag–C_{NN}$ coordination bonds was performed using NBO and NEDA methods, as well as calculations of natural atomic charges and spin populations. NBO analysis shows that the orbital contribution to the energy (E_{orb}) of the

$Ag–C_{NN}$ coordination bonds is large (158 kcal/mol per bond), resulting in significant electron transfer from the NN radical anions to the Ag(I) cation, mainly to its 5s-AO (Figure 6a), while the contribution of back donation (Figure 6b) is small. According to the Mulliken protocol, 0.09e is transferred from each NN fragment to Ag^+ ($q_{nat}(Ag)$ = 0.82). It should be noted that the contributions of α– and β–electrons to E_{orb} (67.5 and 69.7 kcal/mol for main contributions, respectively) are slightly different, which also leads to different transfer of α– and β–electrons, resulting in the spin population of 5s-AO being 0.009 and a total of –0.004 for the five 4d-AOs.

The natural energy decomposition analysis (NEDA) of the binding energy in the $[Ag–(NN)_2]^–$ diradical is complicated by relativistic effects in the inner shell of Ag^+, which leads to very large values of electrical (E_{el}) and core (E_{core}) contributions. The full energy of the $Ag\text{-}C_{NN}$ coordination bond is estimated at 125 kcal/mol with a charge transfer contribution $–E_{CT}$ = 96.5 kcal/mol. The latter term is similar in nature to the orbital stabilization energy ($–E_{orb}$ = 158 kcal/mol) in the NBO procedure. The large difference in their calculated values is most likely due to the calculation of E_{orb} using the second-order perturbation theory and neglecting the destabilizing interaction of the two forming $Ag–C_{NN}$ bonds. Nevertheless, the E_{orb} assessment is very useful as it allows to understand the details, namely that the predominant contribution to bonding is made by the electron transfer from the sp-type NAO of the carbon atom mainly to the 5s orbital of the Ag^+.

References for Supporting Information

1. Grimme, S.; Antony, J.; Ehrlich, S.; Krieg, H. A Consistent and Accurate *Ab Initio* Parametrization of Density Functional Dispersion Correction (DFT-D) for the 94 Elements H-Pu. *J. Chem. Phys.* **2010**, *132*, 154104, doi:10.1063/1.3382344.
2. Zheng, J.; Xu, X.; Truhlar, D.G. Minimally Augmented Karlsruhe Basis Sets. *Theor. Chem. Acc.* **2011**, *128*, 295–305, doi:10.1007/s00214-010-0846-z.
3. Andrae, D.; Häußermann, U.; Dolg, M.; Stoll, H.; Preuß, H. Energy-Adjustedab Initio Pseudopotentials for the Second and Third Row Transition Elements. *Theor. Chim. Acta* **1990**, *77*, 123–141, doi:10.1007/BF01114537.
4. Grimme, S.; Ehrlich, S.; Goerigk, L. Effect of the Damping Function in Dispersion Corrected Density Functional Theory. *J. Comput. Chem.* **2011**, *32*, 1456–1465, doi:10.1002/jcc.21759.
5. Barone, V.; Cossi, M. Quantum Calculation of Molecular Energies and Energy Gradients in Solution by a Conductor Solvent Model. *J. Phys. Chem. A* **1998**, *102*, 1995–2001, doi:10.1021/jp9716997.
6. Neese, F. Software Update: The ORCA Program System—Version 6.0. *WIREs Comput. Mol. Sci.* **2025**, *15*, e70019, doi:10.1002/wcms.70019.
7. Weinhold, F. *Valency and Bonding: A Natural Bond Orbital Donor-Acceptor Perspective*; Cambridge University Press: Cambridge, UK, 2005; ISBN 978-0-521-83128-4.
8. Glendening, E.D.; Landis, C.R.; Weinhold, F. *NBO 7.0*: New Vistas in Localized and Delocalized Chemical Bonding Theory. *J. Comput. Chem.* **2019**, *40*, 2234–2241, doi:10.1002/jcc.25873.
9. Hess, B.A. Relativistic Electronic-Structure Calculations Employing a Two-Component No-Pair Formalism with External-Field Projection Operators. *Phys. Rev. A* **1986**, *33*, 3742–3748, doi:10.1103/PhysRevA.33.3742.
10. Perdew, J.P.; Ernzerhof, M.; Burke, K. Rationale for Mixing Exact Exchange with Density Functional Approximations. *J. Chem. Phys.* **1996**, *105*, 9982–9985, doi:10.1063/1.472933.
11. Adamo, C.; Barone, V. Toward Reliable Density Functional Methods without Adjustable Parameters: The PBE0 Model. *J. Chem. Phys.* **1999**, *110*, 6158–6170, doi:10.1063/1.478522.
12. Rolfes, J.D.; Neese, F.; Pantazis, D.A. ALL-ELECTRON Scalar Relativistic Basis Sets for the Elements Rb–Xe. *J. Comput. Chem.* **2020**, *41*, 1842–1849, doi:10.1002/jcc.26355.
13. Andrienko, G.A. Chemcraft – Graphical Software for Visualization of Quantum Chemistry Computations. See https://www. chemcraftprog.com.

14. Glendening, E.D. Natural Energy Decomposition Analysis: Extension to Density Functional Methods and Analysis of Cooperative Effects in Water Clusters. *J. Phys. Chem. A* **2005**, *109*, 11936–11940, doi:10.1021/jp058209s.
15. Frisch, M.J.; Trucks, G.W.; Schlegel, H.B.; Scuseria, G.E.; Robb, M.A.; Cheeseman, J.R.; Scalmani, G.; Barone, V.; Mennucci, B.; Petersson, G.A.; Nakatsuji, H.; Caricato, M.; Li, X.; Hratchian, H.P.; Izmaylov, A.F.; Bloino, J.; Zheng, G.; Sonnenberg, J.L.; Hada, M.; Ehara, M.; Toyota, K.; Fukuda, R.; Hasegawa, J.; Ishida, M.; Nakajima, T.; Honda, Y.; Kitao, O.; Nakai, H.; Vreven, T.; Montgomery, J.A., Jr.; Peralta, J.E.; Ogliaro, F.; Bearpark, M.; Heyd, J.J.; Brothers, E.; Kudin, K.N.; Staroverov, V.N.; Kobayashi, R.; Normand, J.; Raghavachari, K.; Rendell, A.; Burant, J.C.; Iyengar, S.S.; Tomasi, J.; Cossi, M.; Rega, N.; Millam, N.J.; Klene, M.; Knox, J.E.; Cross, J.B.; Bakken, V.; Adamo, C.; Jaramillo, J.; Gomperts, R.; Stratmann, R.E.; Yazyev, O.; Austin, A. J.; Cammi, R.; Pomelli, C.; Ochterski, J. W.; Martin, R.L.; Morokuma, K.; Zakrzewski, V.G.; Voth, G.A.; Salvador, P.; Dannenberg, J.J.; Dapprich, S.; Daniels, A.D.; Farkas, Ö.; Foresman, J.B.; Ortiz, J.V.; Cioslowski, J.; Fox, D.J. *Gaussian, Inc., Wallingford CT,* **2009**.
16. Tao, J.; Perdew, J.P.; Staroverov, V.N.; Scuseria, G.E. Climbing the Density Functional Ladder: Nonempirical Meta–Generalized Gradient Approximation Designed for Molecules and Solids. *Phys. Rev. Lett.* **2003**, *91*, 146401, doi:10.1103/PhysRevLett.91.146401.
17. Heß, B.A.; Marian, C.M.; Wahlgren, U.; Gropen, O. A Mean-Field Spin-Orbit Method Applicable to Correlated Wavefunctions. *Chem. Phys. Lett.* **1996**, *251*, 365–371, doi:10.1016/0009-2614(96)00119-4.
18. Nagao, H.; Nishino, M.; Shigeta, Y.; Soda, T.; Kitagawa, Y.; Onishi, T.; Yoshioka, Y.; Yamaguchi, K. Theoretical Studies on Effective Spin Interactions, Spin Alignments and Macroscopic Spin Tunneling in Polynuclear Manganese and Related Complexes and Their Mesoscopic Clusters. *Coord. Chem. Rev.* **2000**, *198*, 265–295, doi:10.1016/S0010-8545(00)00231-9.
19. Becke, A.D. Density-Functional Thermochemistry. III. The Role of Exact Exchange. *J. Chem. Phys.* **1993**, *98*, 5648–5652, doi:10.1063/1.464913.
20. Lee, C.; Yang, W.; Parr, R.G. Development of the Colle-Salvetti Correlation-Energy Formula into a Functional of the Electron Density. *Phys. Rev. B* **1988**, *37*, 785–789, doi:10.1103/PhysRevB.37.785.
21. Soda, T.; Kitagawa, Y.; Onishi, T.; Takano, Y.; Shigeta, Y.; Nagao, H.; Yoshioka, Y.; Yamaguchi, K. Ab Initio Computations of Effective Exchange Integrals for H–H, H–He–H

and Mn_2O_2 Complex: Comparison of Broken-Symmetry Approaches. *Chem. Phys. Lett.* **2000**, *319*, 223–230, doi:10.1016/S0009-2614(00)00166-4.

22. Windom, Z.W.; Perera, A.; Bartlett, R.J. Benchmarking Isotropic Hyperfine Coupling Constants Using (QTP) DFT Functionals and Coupled Cluster Theory. *J. Chem. Phys.* **2022**, *156*, 094107, doi:10.1063/5.0069928.
23. Haase, P.A.B.; Repisky, M.; Komorovsky, S.; Bendix, J.; Sauer, S.P.A. Relativistic DFT Calculations of Hyperfine Coupling Constants in 5d Hexafluorido Complexes: $[ReF_6]^{2-}$ and $[IrF_6]^{2-}$. *Chem. – Eur. J.* **2018**, *24*, 5124–5133, doi:10.1002/chem.201704653.